J. Fluid Mech. (1983), *vol.* 133, *pp.* 17–35
Printed in Great Britain

The effect of Brownian diffusion on shear-induced coagulation of colloidal dispersions

By D. L. FEKE† AND W. R. SCHOWALTER
Department of Chemical Engineering, Princeton University, Princeton, New Jersey 08544

(Received 27 April 1982 and in revised form 5 January 1983)

The effect of a small amount of Brownian diffusion on shear-induced coagulation of spherical particles has been calculated. This has been accomplished by considering the binary collision process between a test sphere and identical spheres interacting with the test sphere through induced-dipole attraction, electrostatic repulsion and hydrodynamically induced forces. The effect of diffusion is found by means of an expansion in inverse Péclet number. Specific calculations were performed for uniaxial extension and for laminar shear flow. It is found that Brownian diffusion, the effect of which is nonlinearly coupled with flow type and strength, can act to increase or decrease the coagulation rate.

1. Introduction

Colloidal particles suspended in an aqueous medium may or may not undergo spontaneous coagulation. Electrostatic stabilization of the suspension can occur if ions of similar charge are bound to the particle surfaces. However, induced-dipole attraction between the particles tends to produce agglomerates. In the presence of induced-dipole attraction and electrostatic repulsion two particles typically exhibit modest attraction at large separations, undergo repulsion at intermediate separations, and are strongly attracted at particle–surface separations small relative to the particle radius.

When a colloidal dispersion is subjected to hydrodynamic forces, these may act either to enhance or to inhibit coagulation. Work by van de Ven & Mason (1976) and Zeichner & Schowalter (1977) has shown in considerable detail how the physicochemical and hydrodynamic forces interact and hence affect colloid stability.

When the particles are very small, so that the relative bulk convection of two interacting particles is weak compared with the motion caused by Brownian diffusion, one can neglect macroscopic convective effects, but must account for Brownian motion as a means by which particles are carried towards and away from each other. In aqueous systems, for example, if the particles have a diameter in the neighbourhood of 0.1 μm or less, it is quite likely that bulk hydrodynamics is of no consequence for colloid stability.

Many years ago Smoluchowski (1917) considered the two asymptotic limits of Brownian and shear-induced coagulation. His model for the Brownian case was essentially the diffusion of non-interacting spheres to a test sphere, the dynamics being described by the spherically symmetric portion of the diffusion equation with a uniform diffusivity. From the rate at which particles diffused to the test sphere and

† Present address: Department of Chemical Engineering, Case Western Reserve University, Cleveland, Ohio 44106.

were hence removed from the diffusive process, a coagulation rate was derived in terms of the Stokes–Einstein diffusion coefficient. After assuming that each collision occurred between particles of equal size, Smoluchowski obtained the expression for the frequency j_B^0 of Brownian collisions with a test particle:

$$j_B^0 = \frac{8kTn_\infty}{3\mu}, \tag{1.1}$$

where k is the Boltzmann constant, T the temperature, μ the fluid viscosity, and n_∞ the number density of particles far from the test particle. Smoluchowski made no allowance for the physicochemical forces mentioned above. Refinements to his work are often expressed in terms of a Brownian stability ratio, defined by

$$W_B = \frac{j_B^0}{j_B}, \tag{1.2}$$

where j_B is a coagulation rate including effects of interparticle attraction and repulsion and, in modern work, the effect of particle–particle interaction on the relative diffusivity (see e.g. Spielman 1970).

The asymptotic limit in which Brownian motion is of no consequence relative to bulk convection was also considered by Smoluchowski (1917). In the case of laminar shear flow, $\boldsymbol{v} = (Gy, 0, 0)$, in a suspension of homogeneous spherical particles with radius a, the coagulation rate is given by

$$j_s^0 = \frac{32}{3}a^3Gn_\infty, \tag{1.3}$$

if it is assumed that the particles follow undisturbed streamlines. One can of course also compute similar rates for other types of reference flows, such as pure stretching, where $\boldsymbol{v} = (-Gx, -Gy, 2Gz)$. For these reference flows a ratio W_s is then defined analogously to (1.2).

Coagulation under conditions where bulk convection and Brownian diffusion are simultaneously important is considerably more difficult to describe than the limiting cases given above. Swift & Friedlander (1964) concluded on the basis of their experiments that the two processes were linearly independent over a wide range of conditions. An expansion due to van de Ven & Mason (1977), valid when Brownian effects are large relative to bulk convection, has demonstrated that the Swift & Friedlander hypothesis is not valid in that regime.

In the work presented here we consider the case of convection-dominated colloidal coagulation in the presence of small amounts of Brownian motion. The two prototype flows of steady pure stretching (uniaxial extension) and steady laminar shear flow are examined. It is shown that a regular perturbation expansion for the pair probability density suffices to match the boundary conditions. One finds that in the case of laminar shear flow the tendency of particles to describe non-repeating orbits around a test particle contributes appreciably to the computed value of the coagulation rate. The results for pure stretching and for laminar shearing are different, but in each case it is shown that Brownian and bulk-flow effects are interactive, so that one cannot treat the two contributions as a summation of independent effects.

In §2 we introduce a physical model for the coagulation process, which in this case is considered as a binary interaction between two spheres. Analysis of the two-sphere dynamics is developed in §3, and a presentation and discussion of the results follows in §4.

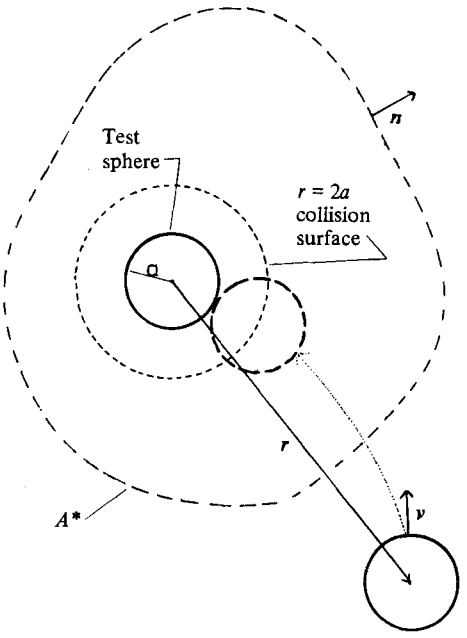

FIGURE 1. Notation for a binary encounter between identical spheres.

2. The physical model

The analysis is restricted to binary interactions in a dilute suspension of identical spheres. Let the origin of a coordinate system coincide with one sphere, which we label as the test sphere. The rate of coagulation j based on the test sphere alone is given by the net influx of particles through some surface A^* which encloses the test sphere, as shown in figure 1. When a particle undergoes coagulation, it is considered to be removed from the system, but particles are supplied to the system at a rate equal to their removal so that the coagulation process is steady in time. The coagulation rate j can be expressed in terms of the steady conditional pair distribution function $P(\boldsymbol{r})$ and the particle velocity $\boldsymbol{v}(\boldsymbol{r})$ relative to the test sphere by

$$j = -\int_{A^*} P(\boldsymbol{r})\, \boldsymbol{v}\cdot\boldsymbol{n}\, \mathrm{d}A, \tag{2.1}$$

where the pair distribution function is defined so that it corresponds to the number density of particles at a position $\boldsymbol{r}$ from the centre of the test sphere. Thus we must know both the particle velocity field and the steady-state pair distribution function in order to predict coagulation kinetics. In the work reported for the limit of no Brownian diffusion (van de Ven & Mason 1976; Zeichner & Schowalter 1977) $P(\boldsymbol{r})$ was known from calculation of particle trajectories, with the condition that the concentration of particles was uniform far upstream from the test sphere. In the present case, solution for $P(\boldsymbol{r})$ is more difficult, because particles undergo Brownian diffusion in any region of non-uniform concentration. The pair distribution function is governed at steady state by

$$\nabla\cdot(\boldsymbol{v}P) = 0 \quad (r \geqslant 2), \tag{2.2}$$

along with appropriate boundary conditions. Here r is the distance from the centre of the test particle, scaled with particle radius. Note that there are three contributions

to the particle velocity $\boldsymbol{v}$. Because we are assuming that inertial effects are unimportant, $\boldsymbol{v}$ can be decomposed into linearly independent contributions from colloidal forces, a hydrodynamic force due to bulk flow, and a Brownian force. Each of these is discussed below.

2.1. *Velocity due to colloidal force*

We shall assume that induced-dipole attraction and electrostatic repulsion are the sole contributors to what we are calling colloidal forces between the particles. Furthermore, we shall assume that these two effects are adequately described by a version of the Derjaguin–Landau–Verwey–Overbeek (DLVO) theory in the form presented by Zeichner & Schowalter (1977). Although inadequacies of the DLVO theory are well documented (see e.g. Pashley 1981), there are realistic situations under which the theory appears to be quite satisfactory (Zeichner & Schowalter 1979).

We employ three separate expressions to describe induced-dipole attraction. Under conditions of no retardation, i.e. no phase lag between dipoles, the Hamaker expression

$$V_A = -\frac{A}{6}\left[\frac{2}{r^2-4}+\frac{2}{r^2}+\ln\frac{r^2-4}{r^2}\right], \tag{2.3}$$

is used, where V_A is the attractive potential, A is Hamaker's constant, and r is the distance between particle centres scaled on the particle radius a. When retardation is important, Schenkel & Kitchener (1960) proposed, as alternatives to (2.3) at small separations,

$$V_A = \frac{-A}{12(r-2)}\left[\frac{1}{1+1.77p}\right] \quad (r-2 \ll 1, p \leqslant 0.57), \tag{2.4}$$

$$V_A = \frac{-A}{r-2}\left[\frac{2.45}{60p}-\frac{2.17}{180p^2}+\frac{0.59}{420p^3}\right] \quad (r-2 \ll 1, p > 0.57). \tag{2.5}$$

For large separations, Kruyt (1949) has presented an approximation in which effects of retardation on the interparticle potential are included, viz

$$V_A = -\frac{16A}{9r^6}\left[\frac{2.45}{p}-\frac{2.04}{p^2}\right] \quad (r \gg 1). \tag{2.6}$$

In these expressions $p = 2\pi(r-2)\,a/\lambda$, where λ is the London wavelength for the particles and is typically of order 0.1 μm. Further refinements, such as a dependence of A on dipole wavelength and on fluid species can be readily accommodated within this framework.

The usual approximations valid for thin double layers, low and uniform surface potential and position-independent dielectric strength lead to a repulsive potential approximated by

$$V_R = \pm\tfrac{1}{2}\epsilon a\psi_0^2 \ln\left[1 \pm \exp\left(-a\kappa(r-2)\right)\right], \tag{2.7}$$

where ϵ is the dielectric strength, ψ_0 the surface potential and $a\kappa \gg 1$, where κ^{-1} is a measure of the thickness of the ion double layer surrounding a particle. Positive signs in (2.7) are used for particles that interact at constant surface potential; the case of constant surface charge can be treated by substituting minus signs where a choice is indicated and relating the surface charge σ_0 to (2.7) by

$$\psi_0 = \frac{4\pi a\sigma_0}{\epsilon(1+a\kappa)}. \tag{2.8}$$

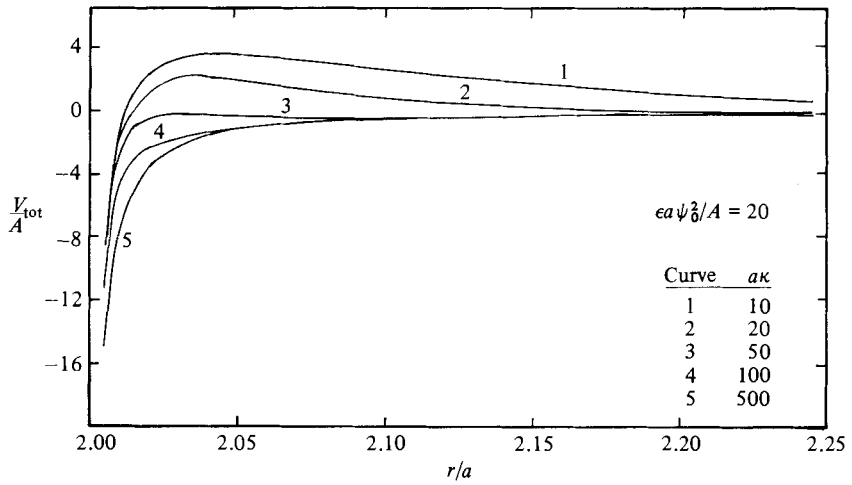

FIGURE 2. Effect of ionic strength on interparticle potential, according to DLVO theory, between identical spheres.

A description of DLVO theory, which is the combination of attractive and repulsive potentials presented above, is available in Sonntag & Strenge (1972). Typical examples of the composite potential $V_{tot} = V_A + V_R$ are shown in figure 2.

The contribution of colloidal forces to the velocity in (2.2) is

$$\boldsymbol{v}_c = \frac{C(r)\,\boldsymbol{F}_c}{6\pi\mu a}, \tag{2.9}$$

where μ is the fluid viscosity and

$$\boldsymbol{F}_c = -\nabla(V_A + V_R) = \frac{A}{a}(f_A + Rpf_R)\,\boldsymbol{e}_r. \tag{2.10}$$

The unit vector $\boldsymbol{e}_r$ is taken along a position vector drawn from the origin at the centre of the test particle to the centre of the particle of interest. $C(r)$ is a separation-dependent relative particle mobility which reflects hydrodynamic interaction between particles. Non-dimensional magnitudes of the forces of attraction and repulsion are given by

$$f_A = -\frac{a}{A}\frac{\mathrm{d}V_A}{\mathrm{d}r},$$

$$f_R = -\frac{1}{\epsilon\psi_0^2}\frac{\mathrm{d}V_R}{\mathrm{d}r},$$

and $Rp = \epsilon\psi_0^2 a/A$ is a *repulsion number*, the magnitude of which is an indication of the strength of repulsion relative to attraction.

2.2. *Velocity due to bulk flow*

The physical model employed in this analysis is based on the interaction of two equal-sized spheres placed in a velocity field which at large distances from the particles is characterized by a velocity $\boldsymbol{u}^0$ varying linearly with position. Thus

$$\boldsymbol{u}^0 = \boldsymbol{\omega} \times \boldsymbol{r} + \boldsymbol{E}\cdot\boldsymbol{r}, \tag{2.11}$$

where $\boldsymbol{\omega} = \frac{1}{2}\nabla \times \boldsymbol{u}^0$ and $\boldsymbol{E} = \frac{1}{2}[\nabla\boldsymbol{u}^0 + (\nabla\boldsymbol{u}^0)^{\mathrm{T}}]$ are the constant ambient spin vector and

rate-of-deformation tensor, respectively. The velocity of a second sphere relative to the test sphere has been found by Batchelor & Green (1972*a*) to be

$$\boldsymbol{v}_{\mathrm{f}} = \boldsymbol{\omega}\times\boldsymbol{r} + \boldsymbol{E}\cdot\boldsymbol{r} - \left\{A(r)\frac{\boldsymbol{rr}}{r^2} + B(r)\left(\boldsymbol{I}-\frac{\boldsymbol{rr}}{r^2}\right)\right\}\cdot\boldsymbol{E}\cdot\boldsymbol{r}, \tag{2.12}$$

where $A(r)$ and $B(r)$ are known functions characterizing hydrodynamic interaction between the particles.

2.3. *Velocity due to Brownian force*

Because we are especially interested in relative motion of spheres at small separations, it is necessary to account for hydrodynamic effects between particles undergoing Brownian diffusion. Batchelor (1976) has shown that in such cases the relative velocity induced by Brownian motion is

$$\boldsymbol{v}_{\mathrm{B}} = -\boldsymbol{D}(\boldsymbol{r})\cdot\boldsymbol{\nabla}\ln P(\boldsymbol{r}), \tag{2.13}$$

where

$$\boldsymbol{D} = \frac{kT}{3\pi\mu a}\left\{G(r)\frac{\boldsymbol{rr}}{r^2} + H(r)\left[\boldsymbol{I}-\frac{\boldsymbol{rr}}{r^2}\right]\right\}. \tag{2.14}$$

The hydrodynamic functions $G(r)$ ($G(r) = \frac{1}{2}C(r)$) and $H(r)$ are known (Batchelor 1976).

2.4. *Governing equation for $P(\boldsymbol{r})$*

We now substitute the expressions (2.9) and (2.13) into

$$\boldsymbol{v} = \boldsymbol{v}_{\mathrm{c}} + \boldsymbol{v}_{\mathrm{f}} + \boldsymbol{v}_{\mathrm{B}}, \tag{2.15}$$

and combine (2.15) with (2.2) to obtain

$$\tilde{\boldsymbol{\nabla}}\cdot\left[\left(\tilde{\boldsymbol{v}}_{\mathrm{f}} + \frac{1}{Fl}C\tilde{\boldsymbol{F}}_{\mathrm{c}}\right)P(\boldsymbol{r})\right] = \frac{1}{Pe}\tilde{\boldsymbol{\nabla}}\cdot(\tilde{\boldsymbol{D}}\cdot\tilde{\boldsymbol{\nabla}}P(\boldsymbol{r})) \quad (r \geqslant 2). \tag{2.16}$$

The tilde refers to dimensionless quantities. Lengths have been scaled on a, velocities on aG, $\boldsymbol{F}_{\mathrm{c}}$ on A/a, and the diffusivity on $kT/3\pi\mu a$. The *flow number* Fl is defined by

$$Fl = \frac{6\pi\mu a^3 G}{A} \tag{2.17}$$

and is a measure of the importance of bulk flow relative to interparticle attraction. The Péclet number

$$Pe = \frac{3\pi\mu a^3 G}{kT} \tag{2.18}$$

reflects the importance of convection relative to Brownian diffusion. In each case G is a scalar measure of the strength of the flow field, such as a multiple of the second invariant of $\boldsymbol{E}$. Because $Fl = (2kT/A)\,Pe$ it is clear that Fl and Pe cannot be varied independently for a given material and temperature. A distinction was preserved between the two dimensionless groups in order to facilitate comparison of results to earlier work in which Fl is finite but Brownian motion is ignored. Because one expects $2kT/A = O(1)$, conditions where $Fl = O(1)$ and $Pe \gg 1$ may not be realizable in practice.

Boundary conditions for (2.16) are

$$\left.\begin{aligned} &P = 0 \quad \text{at} \quad r = 2, \\ &P \to n_\infty \quad \text{as} \quad r \to \infty \text{ upstream}, \\ &\frac{\partial P}{\partial r} \to 0 \quad \text{as} \quad r \to \infty \text{ downstream}. \end{aligned}\right\} \tag{2.19}$$

Upstream and downstream regions, the significance of which will be discussed below, are defined respectively by $\boldsymbol{v}\cdot\boldsymbol{r} < 0$ and $\boldsymbol{v}\cdot\boldsymbol{r} > 0$ as $r \to \infty$. n_∞ is the (spatially homogeneous) number density in the absence of coagulation.

3. Analysis

3.1. *Previous work*

In order to place the present work in its proper context, we indicate how previous analyses of colloidal coagulation can be considered as solutions to special cases of (2.16).

In the case where only Brownian coagulation occurs, i.e. $Fl = Pe = 0$, (2.16) reduces to

$$\tilde{\boldsymbol{\nabla}}\cdot(C\tilde{\boldsymbol{F}}_c P) = \frac{2kT}{A}\tilde{\boldsymbol{\nabla}}\cdot(\tilde{\boldsymbol{D}}\cdot\tilde{\boldsymbol{\nabla}}P). \tag{3.1}$$

Smoluchowski's analysis corresponds to $\tilde{\boldsymbol{F}}_c = \boldsymbol{0}$, and he assumed $\tilde{\boldsymbol{D}} = \boldsymbol{I}$. Then the solution of (3.1) is

$$P = \left(1 - \frac{2}{r}\right) n_\infty. \tag{3.2}$$

Substitution of (3.2) into (2.1) with $\boldsymbol{v} = \boldsymbol{v}_B$ and the additional requirement that collisions are between particles of equal size results in (1.1). The results of Spielman (1970) are recovered by incorporating $\boldsymbol{F}_c$ through (2.10). One obtains

$$W_B = 4\int_2^\infty \frac{\exp\left[\frac{1}{kT}(V_A + V_R)\right]}{r^2 C(r)}\,dr. \tag{3.3}$$

Shear-induced coagulation, as calculated by Smoluchowski, is reproduced if one sets $Pe^{-1} = 0$, $\tilde{\boldsymbol{F}}_c = \boldsymbol{0}$, and $A(r) = B(r) = 0$ in (2.12). Then solution of (2.16) reduces to

$$P = [1 - H(2-r)]\, n_\infty, \tag{3.4}$$

where $H(2-r)$ is the Heaviside step function. Once again, an expression for collision frequency, for example (1.3), is found from substitution of (3.4) and an appropriate velocity function into (2.1).

The results of van de Ven & Mason (1976) and of Zeichner & Schowalter (1977) are also contained in (2.16). They ignored Brownian diffusion ($Pe^{-1} = 0$) but included effects of bulk flow and colloidal forces. As we shall see in §4, when orbiting trajectories are present there can be significant differences between coagulation rates predicted by these workers and those of the present work, in which a more careful analysis is made of the role of those particles undergoing one or more orbits around a test sphere.

3.2. *Method of solution for* $Pe \gg 1$

Our task is to solve (2.16), using the associated equations (2.12) and (2.14), subject to the boundary conditions (2.19). We do this through an expansion

$$P = P_0 + Pe^{-1}P_1 + O(Pe^{-2}). \tag{3.5}$$

Thus we obtain the perturbation equations

$$\tilde{\boldsymbol{\nabla}}\cdot\left[\tilde{\boldsymbol{v}}_f + \frac{1}{Fl}C\tilde{\boldsymbol{F}}_c\right]P_0 = 0, \tag{3.6}$$

$$\tilde{\boldsymbol{\nabla}}\cdot\left[\tilde{\boldsymbol{v}}_f + \frac{1}{Fl}C\tilde{\boldsymbol{F}}_c\right]P_1 = \tilde{\boldsymbol{\nabla}}\cdot(\tilde{\boldsymbol{D}}\cdot\tilde{\boldsymbol{\nabla}}P_0), \tag{3.7}$$

with

$$\left.\begin{aligned} &P_0 = P_1 = 0 \quad \text{at} \quad r = 2, \\ &P_0 = n_\infty, \quad P_1 = 0 \quad \text{as} \quad r \to \infty \text{ upstream}, \\ &\frac{\partial P_0}{\partial r} = \frac{\partial P_1}{\partial r} = 0 \quad \text{as} \quad r \to \infty \text{ downstream}. \end{aligned}\right\} \tag{3.8}$$

From the equation for coagulation rate (2.1),

$$j_0 = -\int_{A^*} (\boldsymbol{v}_f + \boldsymbol{v}_c) \cdot \boldsymbol{n} P_0 \, dA, \tag{3.9}$$

$$j_1 = -\int_{A^*} [(\boldsymbol{v}_f + \boldsymbol{v}_c) P_1 - \boldsymbol{D} \cdot \nabla P_0] \cdot \boldsymbol{n} \, dA, \tag{3.10}$$

where

$$j = j_0 + Pe^{-1} j_1 + O(Pe^{-2}).$$

It is instructive first to inspect the form of solutions to (3.6) and (3.7) in the near- and far-field limits $r-2 \ll 1$ and $r \gg 1$, respectively.

The near-field solution. At $r-2 \ll 1$ one finds that the dominant contribution to (3.6) is from the term containing $C\tilde{\boldsymbol{F}}_c$, which in turn is governed by f_A in (2.10). From (3.2) one finds

$$C\tilde{\boldsymbol{F}}_c = \left[-\frac{1}{3(r-2)} + O(r-2)^{-\frac{1}{2}} \right] \boldsymbol{e}_r, \tag{3.11}$$

where $\boldsymbol{e}_r$ is a unit vector from the test sphere along the line of centres of the two interacting spheres. Substitution of (3.11) into (3.6) then yields

$$P_0 = \tfrac{3}{4} k_0 (r-2) + O(r-2)^{\frac{3}{2}}, \tag{3.12}$$

where k_0 is a constant of integration. Note that this solution ensures that the boundary condition (3.8) for P_0 at $r = 2$ will be met without regard to the choice of integration constant. Substitution of (3.12) into the right-hand side of (3.7) shows that again the contribution of $\boldsymbol{F}_c$ dominates, and an expression for P_1 similar to (3.12) results. Clearly, the boundary condition for $r = 2$ is again satisfied without fixing the constant of integration and one could proceed likewise to find the same near-field form for higher terms in the expansion (3.5). This is a fortunate result because it allows one to proceed with an analysis based upon a regular expansion for P in powers of Pe^{-1}.

The far-field solution. It is apparent from inspection of terms in (3.6) that for $r \gg 1$ the dominant term is that containing $\tilde{\boldsymbol{v}}_f$, and we can write

$$\tilde{\nabla} \cdot (\tilde{\boldsymbol{v}}_f P) = 0, \tag{3.13}$$

which has the solution (Batchelor & Green 1972*b*)

$$P_0 = \frac{K_0}{1 - A(r)} \exp \int_r^\infty \frac{3[B(r') - A(r')]}{r'[1 - A(r')]} \, dr', \tag{3.14}$$

K_0 being an integration constant. Substitution of the far-field approximations for $A(r)$ and $B(r)$, which follow directly from (3.6) of Batchelor & Green (1972*a*), leads to

$$P_0 = K_0 \left[1 + \frac{25}{2r^6} + o(r^{-6}) \right], \tag{3.15}$$

and the upstream boundary condition (3.8) dictates that $K_0 = n_\infty$.

Proceeding with P_1, (3.7) becomes

$$\tilde{\boldsymbol{v}}_f \cdot \tilde{\nabla} P_1 = \tilde{\nabla} \cdot (\tilde{\boldsymbol{D}} \cdot \tilde{\nabla} P_0), \tag{3.16}$$

and it is necessary to specify the nature of the bulk flow by means of the undisturbed velocity gradient $\boldsymbol{G} = \nabla \boldsymbol{u}^0$. Two types of flow were analysed in detail. These were uniaxial extension, defined in rectangular Cartesian coordinates by

$$\boldsymbol{G} = G \begin{bmatrix} -1 & 0 & 0 \\ 0 & -1 & 0 \\ 0 & 0 & 2 \end{bmatrix}, \tag{3.17}$$

and laminar shear flow,

$$\boldsymbol{G} = G \begin{bmatrix} 0 & 1 & 0 \\ 0 & 0 & 0 \\ 0 & 0 & 0 \end{bmatrix}. \tag{3.18}$$

For these two cases it can be shown that

$$P_1 = \frac{125}{324} n_\infty \psi^{-\frac{8}{3}} \left\{ \frac{z\psi^{\frac{8}{3}}}{(\psi + z^3)^3} [15z^6 + 39\psi z^3 - 30\psi^2] + \ln\left(\frac{(z+\psi^{\frac{1}{3}})^3}{z^3+\psi} \right)^5 + \frac{30}{\sqrt{3}} \left[\tan^{-1}\left(\frac{2z-\psi^{\frac{1}{3}}}{\psi^{\frac{1}{3}}\sqrt{3}} \right) + \frac{\pi}{6} \right] \right\} + O(z^{-9}) \tag{3.19}$$

for uniaxial extension, where $\psi = (x^2+y^2)z$ and we have used the form applicable for $z > 0$, and

$$P_1 = \frac{375}{y} \frac{n_\infty}{6(y^2+z^2)} \left\{ \frac{x}{r^6} + \frac{5}{4(y^2+z^2)} \times \left[\frac{x}{r^4} + \frac{3}{2(y^2+z^2)} \left[\frac{x}{r^2} + \frac{1}{(y^2+z^2)^{\frac{1}{2}}} \left(\tan^{-1}\left(\frac{x}{(y^2+z^2)^{\frac{1}{2}}} \right) \pm \frac{\pi}{2} \right) \right] \right] \right\} + O(r^{-9}) \tag{3.20}$$

with $y > 0$ for laminar shear flow. In these equations and henceforth, coordinates are dimensionless. In (3.20) the positive and negative signs correspond to $x < 0$ and $x > 0$ respectively. Equations (3.19) and (3.20) apply to upstream regions of the flow space and are useful in the context of (3.5) only when $Pe^{-1}P_1 \ll P_0$.

The intermediate region. In this region the perturbation equations (3.6) and (3.7) were solved numerically through an adaptation, now briefly described, of the method of characteristics.

The perturbation equations (3.6) and (3.7) can be rewritten in the form

$$F_1 \frac{\partial P_0}{\partial r} + F_2 \frac{\partial P_0}{\partial \theta} + F_3 \frac{\partial P_0}{\partial \phi} = F_4 P_0, \tag{3.21}$$

$$F_1 \frac{\partial P_1}{\partial r} + F_2 \frac{\partial P_1}{\partial \theta} + F_3 \frac{\partial P_1}{\partial \phi} = F_4 P_1 + \tilde{\nabla} \cdot (\tilde{\boldsymbol{D}} \cdot \tilde{\nabla} P_0), \tag{3.22}$$

where

$$F_1 = \left(\tilde{\boldsymbol{v}}_f + \frac{1}{Fl} C \tilde{\boldsymbol{F}}_c \right) \cdot \boldsymbol{e}_r, \quad F_2 = \frac{\tilde{\boldsymbol{v}}_f \cdot \boldsymbol{e}_\theta}{r},$$

$$F_3 = \frac{\tilde{\boldsymbol{v}}_f \cdot \boldsymbol{e}_\phi}{r \sin\theta} \quad F_4 = -\tilde{\nabla} \cdot \left(\tilde{\boldsymbol{v}}_f + \frac{1}{Fl} C \tilde{\boldsymbol{F}}_c \right),$$

$\boldsymbol{e}_r$, $\boldsymbol{e}_\theta$ and $\boldsymbol{e}_\phi$ being unit vectors for a spherical coordinate system. The origin is taken at the centre of the test sphere, and the connection with rectangular Cartesian coordinates is given by $z = r\cos\theta$, $x = r\cos\theta\cos\phi$. Rearranging (3.21) and (3.22) into a coupled system of ordinary differential equations, one obtains

$$\frac{\mathrm{d}r}{F_1} = \frac{\mathrm{d}\theta}{F_2} = \frac{\mathrm{d}\phi}{F_3} = \frac{\mathrm{d}P_0}{F_4 P_0} = \frac{\mathrm{d}P_1}{F_4 P_1 + \tilde{\nabla}\cdot(\tilde{\boldsymbol{D}}\cdot\tilde{\nabla}P_0)}. \tag{3.23}$$

The first two sets of equations in (3.23) represent relative sphere trajectories in the absence of Brownian motion, and since the functions F_i are known P_0 can be calculated along the trajectories. Solutions for P_1 are of course more difficult to obtain because of the presence of $\tilde{\nabla}\cdot(\tilde{\boldsymbol{D}}\cdot\tilde{\nabla}P_0)$. Details of the numerical procedure are contained in appendix B of Feke (1981). We state here only the general steps in the numerical algorithm.

(1) A primary trajectory was chosen by selecting initial coordinates on an upstream portion of the surface A^*. In close proximity to this initial position, coordinates were chosen for five auxiliary trajectories, thus forming a trajectory bundle from which the term $\tilde{\nabla}\cdot(\tilde{\boldsymbol{D}}\cdot\tilde{\nabla}P_0)$ could be estimated. Initial values for P_0 and P_1 were found using the approximate far-field solutions (3.15) and (3.19) or (3.20).

(2) A fourth-order Runge–Kutta method was used to solve for P_0 along each trajectory in a bundle.

(3) A finite-difference approximation was found for $\tilde{\nabla}\cdot(\tilde{\boldsymbol{D}}\cdot\tilde{\nabla}P_0)$ along the primary trajectory.

(4) From the last equation of (3.23), P_1 was calculated by using a generalized multistep method.

(5) When the primary trajectory reached the collision surface, $r = 2$, or passed downstream through A^*, the calculation was terminated. (See §3.4 for exceptions.)

(6) Steps (1)–(5) were repeated until P_0 and P_1 were known for a sufficient number of positions to permit calculation of j from (2.1).

3.3. *Uniaxial extension*

Because there is no component of $\tilde{\boldsymbol{v}}_f$ in the ϕ-direction for the undisturbed flow given by (3.17), (3.21) and (3.22) are two-dimensional, and only three trajectories are needed for each bundle. Several base characteristics (particle trajectories for $Pe^{-1} = 0$) are shown in figure 3. The solution is of course symmetric about the plane $\theta = \frac{1}{2}\pi$. The dashed curve separating upstream and downstream regions is given by

$$F_1(r,\theta) = (1-A(r))\,r(3\cos^2\theta - 1) + \frac{C(r)\,\tilde{\boldsymbol{F}}_c\cdot\boldsymbol{e}_r}{Fl} = 0, \tag{3.24}$$

where the point (r^*, θ^*) is on the surface A^*. Identification of the curve with the upstream–downstream division is of course completely correct only in the P_0 approximation, but the change due to a Brownian force should not affect the calculation at $O(Pe^{-1})$.

The limiting trajectory, which separates coagulating and noncoagulating encounters, is found by selecting an initial condition very near to $\theta = 0$, $r = 2$, and integrating backwards. In this way $\theta_{\lim}$ is found, and collision can be expected for all $\theta_{\lim} < \theta \leqslant \frac{1}{2}\pi$. In most integrations, $r^* = 10$ was used, and far-field forms were used to initialize P_0 and P_1 along the characteristics.

Lines of constant P_0, scaled on n_∞, are shown in figure 4 for the case $Fl = 1.0$, $Rp = 0$. As one would expect, a maximum exists for P_0, and the maximum occurs at $\theta = \frac{1}{2}\pi$ and $r \approx 2.65$. In the wake of the test sphere ($\theta \approx 0$) P_0 drops significantly below

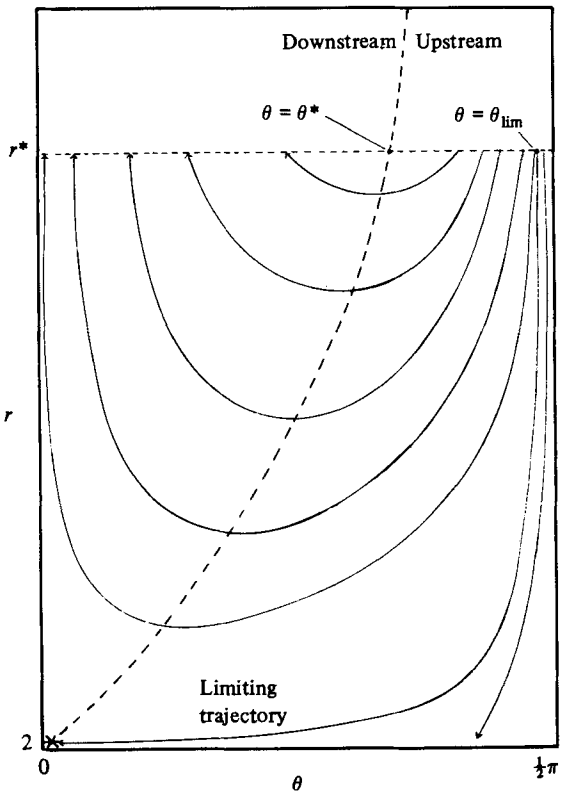

FIGURE 3. Typical relative trajectories in the uniaxial extension problem. The dashed line, passing through the surface A^* at $r = r^*$ and $\theta = \theta^*$ separates upstream from downstream regions of space. The limiting trajectory separates colliding from non-colliding trajectories.

unity, an expected result. The effect of diffusion is shown in figure 5, where we have schematically indicated departures of trajectories from the base characteristics due to the presence of diffusion. Again, as one would expect from intuition and from figure 4, diffusion effects are minimal at large particle separations because of the homogeneity of the distribution function.

3.4. *Laminar shear flow*

Solution for this case is substantially more difficult than for uniaxial extension, the flow now being three-dimensional, although there is symmetry between the first and third, and second and fourth quadrants of the (x, y)-plane.

It is well known that in the absence of diffusion and interparticle forces, there are some closed trajectories of particles orbiting around the test particle. Similar closed trajectories do not exist when interparticle forces are included. Although trajectories may involve multiple circulations around the test particle, the trajectory may spiral inward toward eventual coagulation, or outward, the ultimate result being a downstream path toward infinite separation. In figure 6 we have shown the locus of orbiting trajectories, for $Rp = 0$, as they pass through the integration surface A^*. One can identify two modes of particle orbits. In mode 1 the particle intersects A^* more than once on its way to capture or release. In mode 2 there is only a single intersection with A^*, but there are multiple circuits around the polar axis as the particle moves towards capture. Obviously, the number of orbiting trajectories in

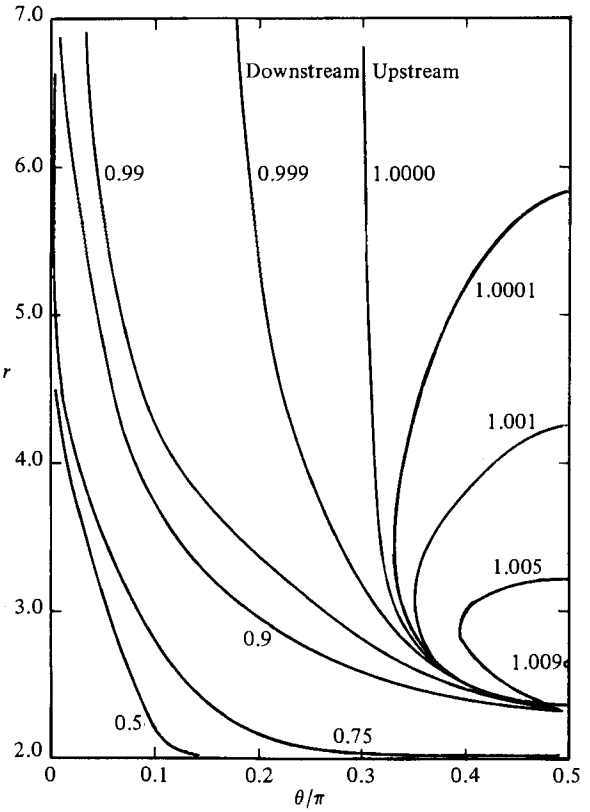

FIGURE 4. Contours of constant P_0 in uniaxial extension. $Fl = 1$, $Rp = 0$. Values of P_0 are scaled on n_∞.

each mode depends on the radius defining A^*. In principle, values of P_0 and P_1 can be calculated just as they were in 3.3. However, the complications introduced by orbiting trajectories are substantial. For example, in order to initialize calculations with the far-field forms of P_0 and P_1, one wishes to pick a point corresponding to a particle that has not already made one or more circuits around the test particle. In addition, a trajectory bundle which at the point of initialization is satisfactorily clustered to permit estimation of the term $\tilde{\nabla} \cdot (\tilde{\boldsymbol{D}} \cdot \tilde{\nabla} P_0)$, may, upon one or more orbits, become too disperse.

As in the case of extensional flow, certain trajectories have special significance. These trajectories can be associated with the first two characteristic equations of (3.23) if, for the moment, we ignore the effect of Brownian motion on trajectories. For example, consider the equatorial plane ((x, y)-plane) for the case of a purely attractive interparticle potential. Representative particle paths are shown in figure 7. Consider the trajectory that passes through the point $r = r^*, \phi = 0$. The history of the particle associated with this trajectory can be found by integrating the characteristic equations backwards until the particle is upstream. Clearly, this is a dividing trajectory in the sense that particles with initial coordinates $\phi' < \phi < \pi$ will not again penetrate A^* before capture.

It is also possible to identify a limiting trajectory that separates coagulating from noncoagulating particles. Since all orbiting trajectories eventually result in coagulation for the case of a purely attractive interparticle potential, the limiting trajectory separates open from orbiting trajectories. This trajectory is identified in

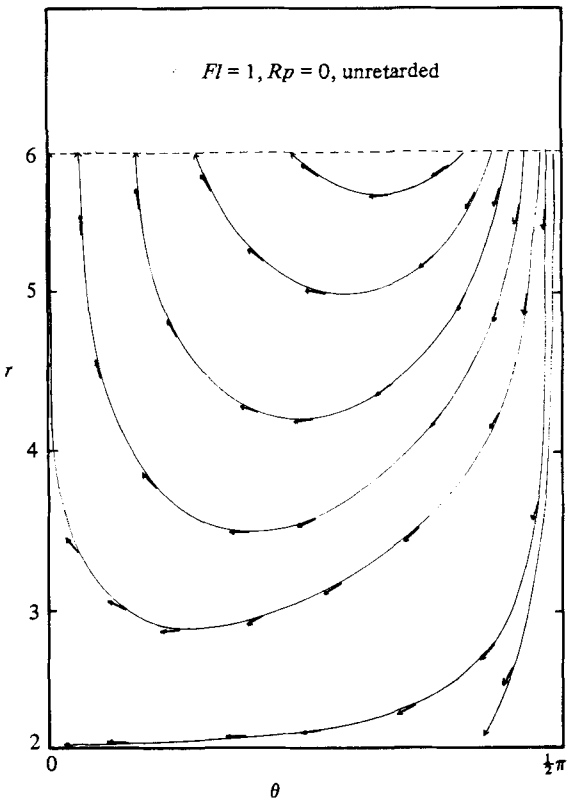

FIGURE 5. Effect on Brownian diffusion on particle trajectories in uniaxial extension. Arrows superposed on the base trajectories represent the relative velocity including diffusion.

figure 7 by $\phi = \phi_{\lim}$ at $r = r^*$ upstream. Thus choice of an initial value of ϕ on r^* such that $\frac{1}{2}\pi < \phi < \phi_{\lim}$ results in an open trajectory. Mode 1 orbiting trajectories are found for initial coordinates $r = r^*$, $\phi_{\lim} < \phi < \phi'$. By means of the value $\phi = \phi^*$ in the second quadrant, we identify those trajectories which are re-entering the test surface. Thus one notes from figure 7 that trajectories with initial coordinates $r = r^*, \phi_{\lim} < \phi < \phi'$ pass back into A^* at $\phi^* - \pi < \phi < 0$. By symmetry, values of the distribution functions for this region of space must be identical to values at the corresponding positions $\phi^* < \phi < \pi$. Thus $r = r^*, \phi = \phi^*$ separates upstream and downstream regions. Trajectories passing through A^* with $\frac{1}{2}\pi < \phi < \phi^*$ are coming from upstream regions of space. Trajectories intersecting A^* with $\phi^* < \phi < \pi$ have initial upstream coordinates on A^* with $\phi_{\lim} - \pi < \phi < \phi' - \pi$.

The first step in the numerical procedure was to identify ϕ'. This was done by integrating backwards the trajectory† crossing A^* with $\phi = 0$. As one considers planes other than the equatorial plane, $\phi' = \phi'(\theta)$. After $\phi'(\theta)$ had been identified, approximately 100 initial trajectory coordinates were selected at $r = r^*$, $0 < \theta < \frac{1}{2}\pi$ and $\frac{1}{2}\pi < \phi < \phi'(\theta)$. Initial values of P_0 and P_1 were assigned from (3.15) and (3.20) to each trajectory in the bundle. Probability densities were calculated along the characteristics until all trajectories passed through the downstream side of A^*. For those trajectories with initial coordinates $\phi_{\lim}(\theta) < \phi < \phi'(\theta)$, the calculation was

† It is convenient to continue to call the base characteristic curves *trajectories*, even though they actually correspond to particle paths only in the limit $Pe = \infty$.

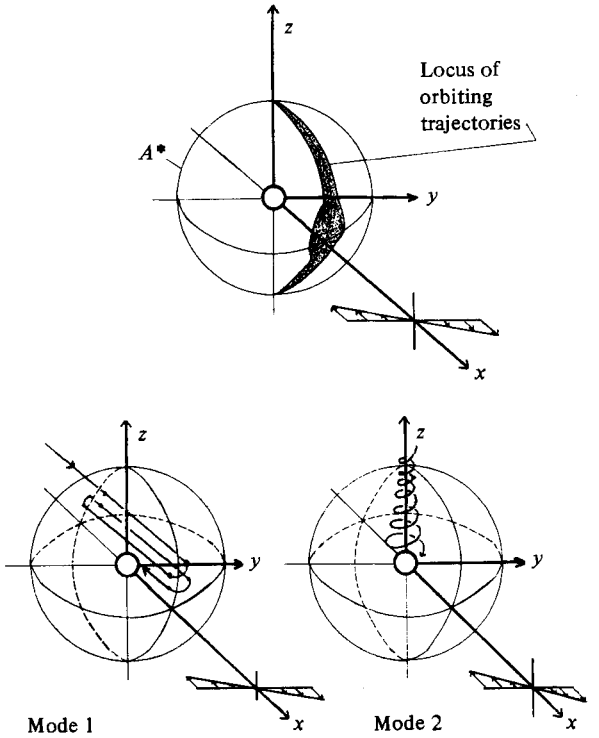

FIGURE 6. Possible orbiting trajectories in laminar shear flow. Trajectories of mode 1 repeatedly penetrate the integration surface. Those of mode 2 penetrate only once.

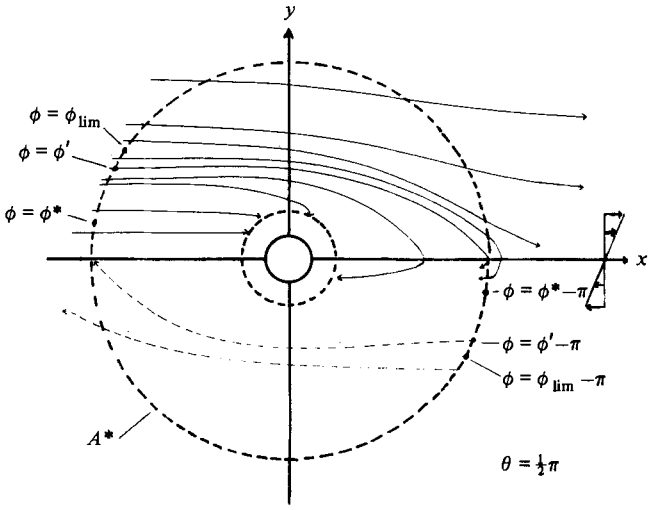

FIGURE 7. Representative trajectories in laminar shear flow for $Rp = 0$. Upstream regions for $y > 0$ are given by $\frac{1}{2}\pi < \phi < \phi^*$. Trajectories intersecting A^* in the region $\phi_{\text{lim}} < \phi < \phi'$ correspond to mode-1 orbiting trajectories.

continued until the trajectories entered the integration surface a second time, at which point the calculation was terminated. Values of P_0 and P_1 on the integration surface were used in the flux calculations.

For the results reported here a value of $r^* = 10$ was used, and ϕ_{lim} was found by continuing calculations on the downstream side of A^* to $r = 15$. If the trajectory had

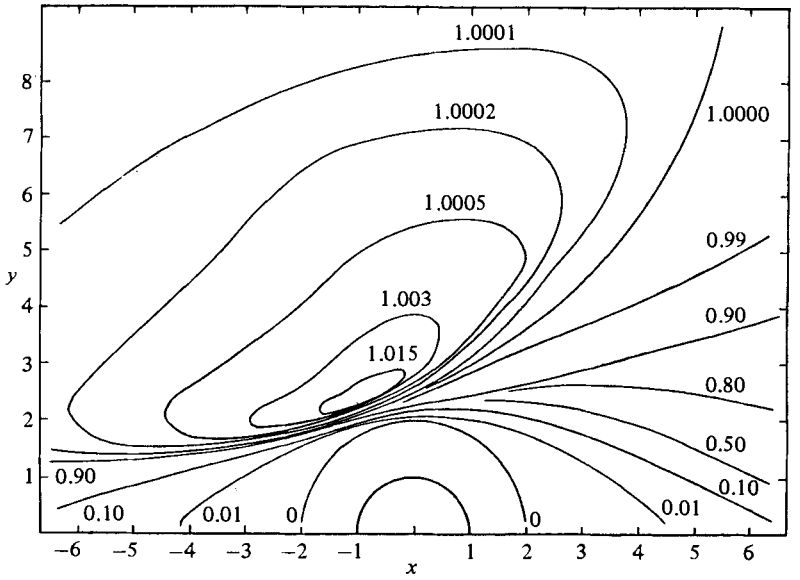

FIGURE 8. Contours of constant P_0, scaled on n_∞, in laminar shear flow. $Fl = 1$, $Rp = 0$.

not reversed direction, it was assumed that the initial value of ϕ was such that $\phi < \phi_{\text{lim}}$.

For comparison with the case of uniaxial extension, we show in figure 8 several contours of P_0 in the equatorial plane for laminar shear flow with $Rp = 0, Fl = 1$.

4. Results and discussion

With the spatial variation of $P(\boldsymbol{r})$ known over the surface A^*, one is in a position to perform the kinetic calculation (2.1). It is useful to consider it in terms of the contributions from (3.9) and (3.10) so that, to order Pe^{-1},

$$j = j_0 + Pe^{-1} j_1. \tag{4.1}$$

For uniaxial extension, representative results are shown in figures 9 and 10. In the latter case, although a modest amount of repulsion is present in the colloidal force ($Rp = 1$), there is no secondary minimum in the potential curve corresponding to figure 2.

Perhaps the most surprising result shown in the figures is the indication that diffusion can act to increase or to decrease coagulation rate as the flow number Fl is increased. This seems to be a consequence of the spatial variation of probability distribution function and the resultant diffusion of particles down the probability density gradient. Consider, for example, the base characteristics and corresponding regions of high and low probability density shown in figure 11. The P_1 correction accounts for diffusion of particles into the regions labelled $P_0 \ll 1$, from which they will tend to be convected downstream without collection. Clearly, this is a process which interacts closely with the strength of the basic flow, and one can imagine situations where the overall effect is to enhance or to decrease coagulation.

Qualitatively similar results are shown for simple laminar shear flow in figure 12. In both cases it is immediately seen that the idea of additivity, suggested by Swift & Friedlander (1964) and referred to earlier, does not apply. There can be strong coupling between flow strength and the action of Brownian motion.

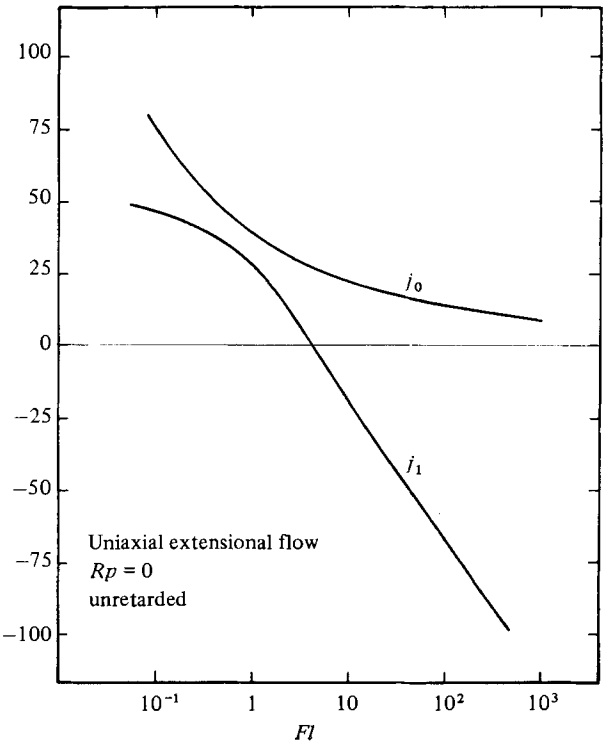

FIGURE 9. Predicted coagulation rates for uniaxial extensional flow. $Rp = 0$. Values of j_0 and j_1 have been scaled on a^3Gn_∞.

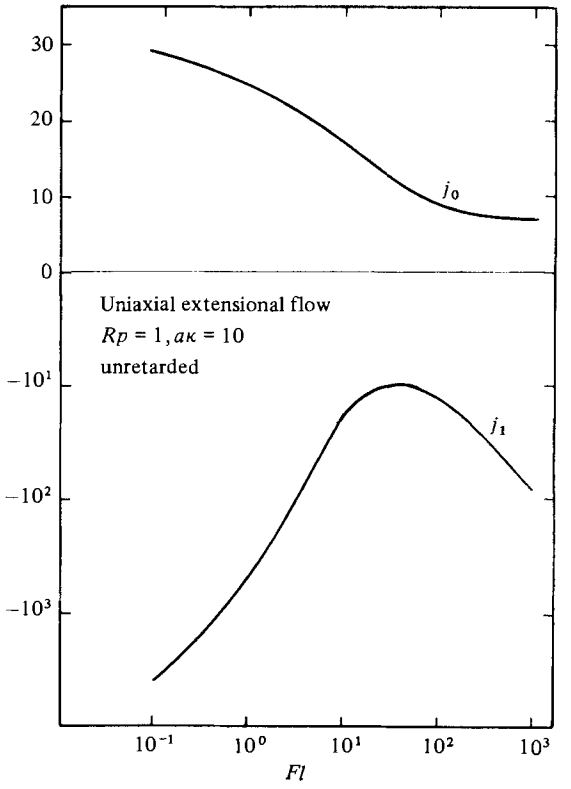

FIGURE 10. Predicted coagulation rates for uniaxial extensional flow, $Rp = 1$, $a\kappa = 10$. Values of j_0 and j_1 have been scaled on a^3Gn_∞.

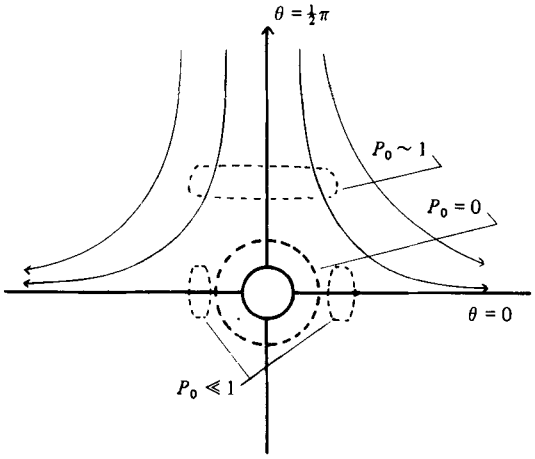

FIGURE 11. Redistribution of particles due to diffusion.

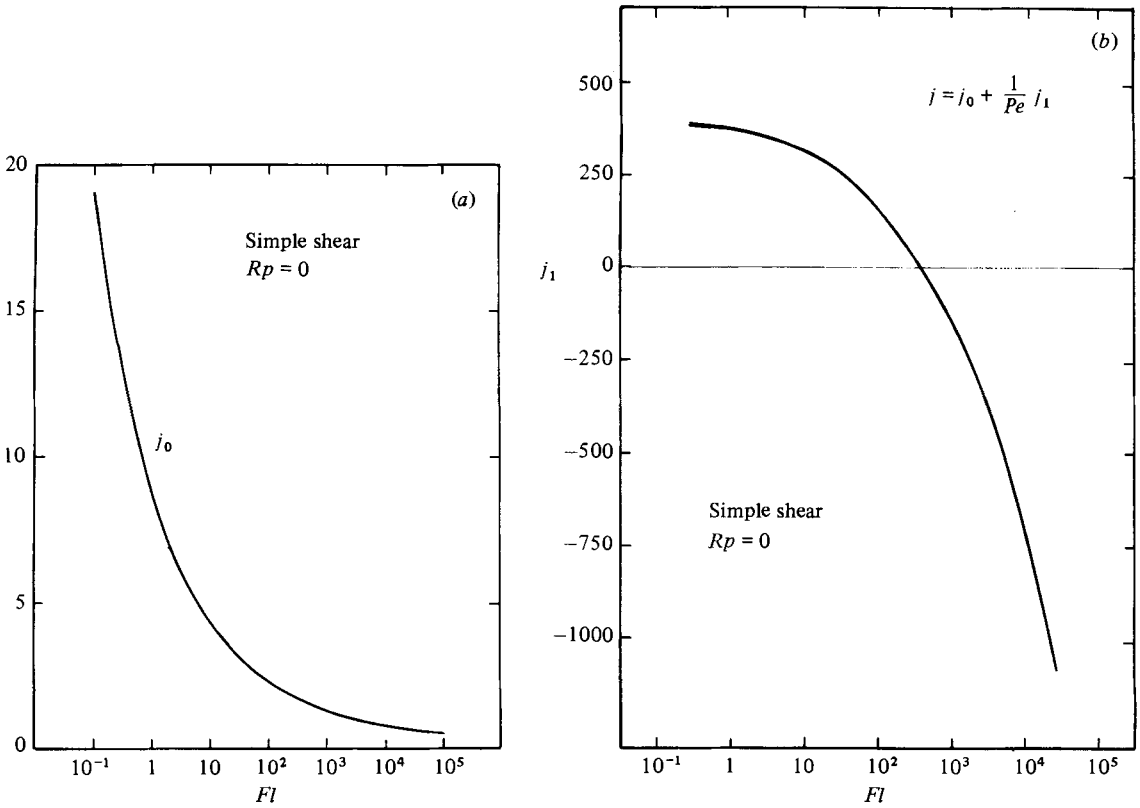

FIGURE 12. Predicted coagulation rates for laminar shear flow. $Rp = 0$, and j_0 and j_1 have been scaled on a^3Gn_∞. (*a*) j_0. (*b*) j_1.

An attempt was made to assess the sensitivity of the results to numerical approximations. Maximum propagated error in the probability function (scaled on n_∞) is estimated to be 10^{-4}. It was found that an initial trajectory bundle contained in a circle centred at the primary trajectory and with radius $O(10^{-6}a)$ provided the best balance between truncation and roundoff error in the calculation of $\tilde{\nabla} \cdot (\tilde{\boldsymbol{D}} \cdot \tilde{\nabla} P_0)$.

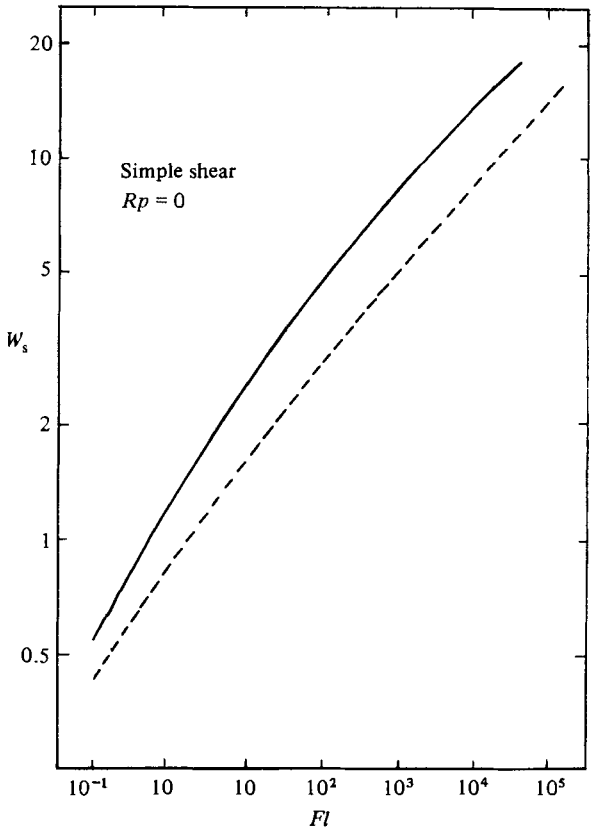

FIGURE 13. Comparison of stability ratios W_s for flow-induced coagulation ($Pe^{-1} = 0$). ---, trajectory analysis of Zeichner & Schowalter (1977); ——, from j_0 of present work.

By comparing results for different placements of the trajectory bundles, some idea of the error in the calculation of j was possible. For extensional flow, errors in j_0 and j_1 are believed to be within $\pm 0.1\,\%$ and $\pm 1\,\%$ respectively. The same quantities for laminar shear flow are estimated to be $\pm 1\,\%$ and $\pm 7\,\%$ respectively.

Finally, we comment on comparison of the present values of j_0 with those of Zeichner & Schowalter (1977). The two approaches coincide for extensional flow. In the case of laminar shearing, the results show measurable differences. These are indicated in plots of stability ratio for $Pe^{-1} = 0$ shown in figure 13. Aside from a minor numerical error in the earlier work (see Feke 1981), the difference is believed to be due to the effect of orbiting particles. In the earlier analysis, coagulation rates were computed without provision for mode-1 orbiting trajectories (figure 6). As a result, coagulation rates were overestimated.

In conclusion, the present work provides an indication of how small amounts of Brownian diffusion will affect a predominantly shear-induced coagulation process. One notes that the interaction between the two processes is complex, hydrodynamics dictating to a large degree the spatial change of the pair distribution function and the time during which a given particle approaching a test particle will be subject to the forces induced by a non-homogeneous probability function.

The authors are grateful to the Xerox Corporation for partial support of this research. D. L. Feke was the recipient of a National Science Foundation predoctoral fellowship.

REFERENCES

BATCHELOR, G. K. 1976 Brownian diffusion of particles with hydrodynamic interaction. *J. Fluid Mech.* **74**, 1–29.

BATCHELOR, G. K. & GREEN, J. T. 1972*a* The hydrodynamic interaction of two small freely-moving spheres in a linear flow field. *J. Fluid Mech.* **56**, 375–400.

BATCHELOR, G. K. & GREEN, J. T. 1972*b* The determination of the bulk stress in a suspension of spherical particles to order c^2. *J. Fluid Mech.* **56**, 401–427.

FEKE, D. L. 1981 Kinetics of flow-induced coagulation with weak Brownian diffusion. Ph.D. thesis, Princeton University.

KRUYT, H. R. 1949 *Colloid Science*, vol. 1, p. 266. Elsevier.

PASHLEY, R. M. 1981 Hydration forces between mica surfaces in aqueous electrolyte solutions. *J. Colloid Interface Sci.* **80**, 153–162.

SCHENKEL, J. H. & KITCHENER, J. A. 1960 A test of the Derjaguin–Verwey–Overbeek theory with a colloidal suspension. *Trans. Faraday Soc.* **56**, 161–173.

SMOLUCHOWSKI, M. VON 1918 Versuch einer mathematischen theorie der koagulationskinetik kolloider lösungen. *Z. Phys. Chem.* **92**, 129–168.

SPIELMAN, L. A. 1970 Viscous interactions in Brownian coagulation. *J. Colloid Interface Sci.* **33**, 562–571.

SWIFT, D. L. & FRIEDLANDER, S. K. 1964 The coagulation of hydrosols by Brownian motion and laminar shear flow. *J. Colloid Sci.* **19**, 621–647.

VEN, T. G. M. VAN DE & MASON, S. G. 1976 The microrheology of colloidal dispersions. IV. Pairs of interacting spheres in shear flow. *J. Colloid Interface Sci.* **57**, 505–516.

VEN, T. G. M. VAN DE & MASON, S. G. 1977 The microrheology of colloidal dispersions. VIII. Effect of shear on perikinetic doublet formation. *Colloid Polymer Sci.* **255**, 794–804.

ZEICHNER, G. R. & SCHOWALTER, W. R. 1977 Use of trajectory analysis to study stability of colloidal dispersions in flow fields. *AIChE J.* **23**, 243–254.

ZEICHNER, G. R. & SCHOWALTER, W. R. 1979 Effects of hydrodynamic and colloidal forces on the coagulation of dispersions. *J. Colloid Interface Sci.* **71**, 237–253.